

# Surface Plasmon-Enhanced Nanopillar Photodetectors

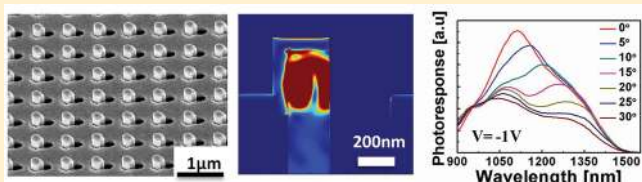
Pradeep Senanayake,<sup>\*,†</sup> Chung-Hong Hung,<sup>†</sup> Joshua Shapiro,<sup>†</sup> Andrew Lin,<sup>†</sup> Baolai Liang,<sup>‡</sup> Benjamin S. Williams,<sup>†,‡</sup> and D. L. Huffaker<sup>†,‡</sup>

<sup>†</sup>Department of Electrical Engineering and <sup>‡</sup>California Nano-Systems Institute, University of California Los Angeles, Los Angeles, California 90095, United States

**S** Supporting Information

**ABSTRACT:** We demonstrate nanopillar- (NP) based plasmon-enhanced photodetectors (NP-PEPDs) operating in the near-infrared spectral regime. A novel fabrication technique produces subwavelength elongated nanoholes in a metal surface self-aligned to patterned NP arrays that acts as a 2D plasmonic crystal. Surface plasmon Polariton Bloch waves (SPP-BWs) are excited by the metal nanohole array resulting in electric field intensity “hot spots” in the NP. The NP periodicity determines the peak responsivity wavelength while the nanohole asymmetry produces polarization-dependent coupling of the SPP-BW modes. Resulting photodetectors have 0.28 A/W responsivity peaked at 1100 nm at a reverse bias of  $-5$  V. Designs for further increasing the optical coupling efficiency into the nanopillar are explored. This technology has potential applications for plasmonically enhanced focal plane arrays and plasmonic photovoltaics.

**KEYWORDS:** Surface plasmons, nanopillar, photodetector arrays, extraordinary optical transmission



Semiconductor nanowires (NWs) and nanopillars (NPs) are an attractive route for miniaturization and III–V/Si integration of various types of electronic and photonic devices. The vertical orientation of these nanostructures facilitates both axial<sup>1,2</sup> and coreshell<sup>3,4</sup> p-n junctions that offer intriguing possibilities for device design and system architectures. For photodetectors and photovoltaics, the large surface area of radial NP junctions allows for greater absorbing volume enhancing carrier absorption and collection.<sup>5</sup> To date, several photodetectors have been reported with promising characteristics such as single and NP arrays with photoconductive gain,<sup>6,7</sup> and high-speed single NW devices.<sup>8,9</sup> The majority of recent device demonstrations are based on self-assembled synthesis, which results in highly nonuniform NWs, which vary in placement, diameter, and height, and are often difficult to integrate into realistic device structures.

Device performance in a NW photodetector is often limited by the challenge of making good electrical contacts to the NWs using a material that is also sufficiently transparent to allow efficient optical coupling. Transparent conducting oxides like indium tin oxide (ITO), and aluminum zinc oxide (AZO) form Schottky barriers<sup>6,10</sup> with GaAs, while ohmic metal contacts are not sufficiently transparent. Metal layers patterned with periodic nanohole arrays offer good electrical contacting while leveraging the phenomenon of extraordinary optical transmission and plasmonic field enhancement for efficient absorption in the NP.<sup>11,12</sup> The benefit of a plasmonic enhanced photodetector is the effective collection of light from a large optical area onto a photodetector junction of much smaller (even subwavelength) area. In principle, this smaller junction area can lead to improved signal-to-noise (detectivity), higher speed operation, and/or reduced material growth requirements. The vertical geometry of a NP is particularly conducive to plasmonically enhanced absorption provided the electric field

intensity can be tightly confined in the NP junction region, and the depletion region in the NP can be optimized for carrier extraction. In contrast, surface plasmon (SP) enhancement in planar photodetectors is limited by the shallow penetration depth of the electric field intensity into the detector absorption region. Plasmonically enhanced photodetectors have been demonstrated in the mid-infrared ( $\lambda \sim 9 \mu\text{m}$ ) using metallic hole arrays<sup>13</sup> in the near-infrared ( $\sim 800$  nm) using bullseye antennas,<sup>14</sup> grating lenses<sup>15</sup> and dipole antennas,<sup>16</sup> and in the visible using C-shaped nanoantennas.<sup>17</sup> Plasmonically enhanced solar cells rely on broadband absorption enhancements in the solar spectrum produced by the scattering of metallic nanoparticles<sup>18</sup> or plasmonic modes supported by different metallic grating configurations.<sup>19,20</sup>

In this work, we demonstrate a metal nanohole array self-aligned to patterned NPs to realize NP plasmon-enhanced photodetectors (NP-PEPDs). The self-aligned nanoholes are fabricated by evaporating the top contact metallization at an off-normal angle, so that the NP tip itself acts as a shadow mask. This eliminates the need for process-intensive lithography to separately define the subwavelength gold nanoholes. The periodicity of the metal nanohole array supports surface plasmon polariton Bloch waves (SPP-BW) resonances, which cannot be realized by randomly oriented NPs. Further enhancement can be achieved with the localized surface plasmon (LSP) resonance produced by the specific shape of the subwavelength nanohole. Together the SPP-BW and LSP resonances can be engineered for enhanced photodetection at any desired wavelength.

**Received:** August 6, 2011

**Revised:** October 29, 2011

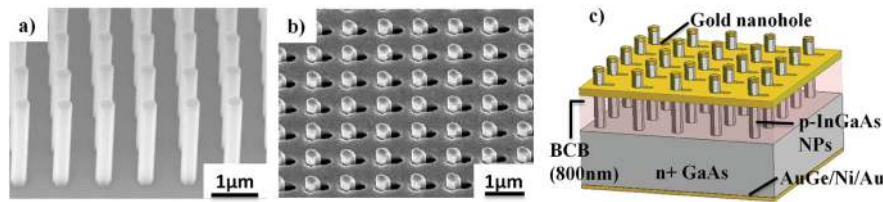


**Figure 1.** (a)  $\text{In}_{0.4}\text{Ga}_{0.6}\text{As}$  NPs grown on  $n^+$  GaAs by selective area MOCVD arranged in a square lattice with a  $1\ \mu\text{m}$  pitch. (b) Tilted SEM at  $52^\circ$  of the gold coated NPs. (c) Schematic of the NP photodetector array.

For the devices studied here,  $p$ -doped  $\text{In}_{0.4}\text{Ga}_{0.6}\text{As}$  NPs are grown by selective-area epitaxy (SAE) on  $n^+$  doped GaAs (111) B substrates at  $10^{18}\ \text{cm}^{-3}$ . Figure 1a shows a typical NP array before processing, and Figure 1b shows an SEM image of the fully processed photodiode array. A schematic of the final device is shown in Figure 1c. The NPs have a height of  $1.3\ \mu\text{m}$ , a diameter of  $200\ \text{nm}$ , and are arranged in a  $1\ \mu\text{m}$  pitch square lattice. The NP doping concentration is estimated to be  $5 \times 10^{17}\ \text{cm}^{-3}$  from single pillar resistivity measurements. A more detailed description of substrate patterning and NP epitaxy are published elsewhere.<sup>21</sup>

Following epitaxy, the NP array is planarized using benzocyclobutene (BCB), which is hard-cured and etched back to expose  $\sim 500\ \text{nm}$  of the NP tips. The top metal contact (Cr,  $20\ \text{nm}$ ; Au,  $200\ \text{nm}$ ) is evaporated at  $35^\circ$  from the substrate normal to coat both top and the exposed side of each NP along with the entire surface interconnecting the pillars. The NP “shadow” leaves the other pillar side uncoated and forms a self-aligned nanohole adjacent to each NP. The nanohole length depends on the exposed tip length and the incident angle of metal deposition, while the nanohole width is defined by the NP diameter. In this work, the resulting nanoholes are  $260\ \text{nm}$  wide and  $315\ \text{nm}$  long. This metal nanohole array forms a 2D plasmonic crystal self-aligned to the NPs. Each NP-PEPD is  $500\ \mu\text{m} \times 500\ \mu\text{m}$  in area with a pitch of  $1\ \mu\text{m}$ . For comparison, an otherwise identical device was also fabricated with a uniform ITO top contact instead of the Cr/Au nanohole array. The ITO device serves as a control to isolate the effect of the Cr/Au nanohole array. After fabrication, the NP-PEPDs are wire bonded to a leadless chip carrier for electrical and optical characterization.

Propagating electromagnetic energy can be coupled into the NP through the nanoholes in the gold top contact via SPP modes supported by the metal nanohole array. A first order approximation of the SPP-BW resonances in the nanopillar can be described by eq 1, where  $P$  is the pitch of the hole array,  $\epsilon_m$  is the dielectric constant of the metal,  $\epsilon_d$  is the dielectric constant of the dielectric medium, and  $(i, j)$  are the scattering orders of the hole array in the  $x$ - and  $y$ -directions<sup>22,23</sup>

$$\lambda_m = \frac{P}{\sqrt{i^2 + j^2}} \text{Re} \left( \sqrt{\frac{\epsilon_m \epsilon_d}{\epsilon_m + \epsilon_d}} \right) \quad (1)$$

This equation describes the conservation of momentum condition necessary to couple normally incident radiation to propagating SPP-BW modes on a metal/dielectric interface. Equation 1 can be instructive in identifying different orders of the surface plasmon modes excited by the metal nanohole array. For the device studied here, this model predicts the  $\text{SP}_{(0,\pm 1)}$  and  $\text{SP}_{(\pm 1,\pm 1)}$  resonances at  $\lambda = 1466\ \text{nm}$  and  $\lambda = 1049\ \text{nm}$  respectively, where  $\epsilon_d = 2.56$  (BCB),  $P = 1\ \mu\text{m}$ , and the dielectric constant of gold,  $\epsilon_m(\lambda)$  is interpolated from experimental values published by Johnson and Christy.<sup>24</sup>

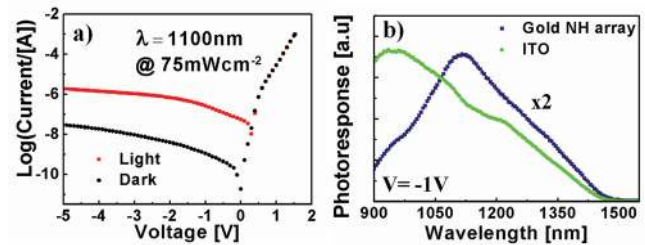


**Figure 2.** (a) Dark and light  $I$ – $V$  characteristics of gold NH device. (b) Photoreponse of NP/NH photodetector showing  $\text{SP}_{(\pm 1,\pm 1)}$  modes, and control device with ITO top contact.

The phenomenon of extraordinary optical transmission involves propagating SPP-BW modes coupling to localized modes of the individual nanohole. These nanohole modes in turn excite similar modes on the other side of the metal film that create a propagating wave in the far-field. In our geometry, we want to exploit the localized “hot spots” of enhanced electric field, such that they have the appropriate spatial and spectral overlap to enhance absorption within the NPs.<sup>25,26</sup> We note that while the first order resonance  $\text{SP}_{(0,\pm 1)}$  is just longer than the cutoff wavelength of the  $\text{In}_{0.4}\text{Ga}_{0.6}\text{As}$  material enhanced photoresponse near  $1050\ \text{nm}$  due to the  $\text{SP}_{(\pm 1,\pm 1)}$  mode is expected to be observable.

The NP photodiode current–voltage ( $I$ – $V$ ) characteristic is measured under dark and light conditions with the Agilent 4156C semiconductor parameter analyzer. The  $I$ – $V$  characteristic is typical of a photovoltaic detector as shown in Figure 2a. The depletion region of the photodiode is located at the interface between the  $p$ -type InGaAs NP and the  $n^+$  GaAs substrate. The ideality factor of the diode is 1.9, while the rectification ratio at  $\pm 1\ \text{V}$  is  $>10^4$ . Under dark conditions, the reverse leakage current of  $30\ \text{nA}$  at  $-5\ \text{V}$  indicates high quality material including low threading dislocations density at the NP-substrate interface. Under illumination ( $\lambda = 1100\ \text{nm}$  at  $75\ \text{mW cm}^{-2}$ ), a responsivity of  $0.28\ \text{A/W}$  is measured at  $-5\ \text{V}$ . The spectral response of the device is measured using light from a quartz tungsten halogen lamp dispersed by a grating monochromator followed by a depolarizer. The depolarizer is necessary to remove the polarization dependence of the monochromator grating. Photocurrent from the devices is measured using a lock-in amplification technique. Figure 2b shows the spectral response of the gold nanohole device and the ITO control device, where both devices are reverse biased at  $-1\ \text{V}$ . At  $1100\ \text{nm}$ , a responsivity of  $0.06\ \text{A/W}$  is measured for the ITO, while a responsivity of  $0.04\ \text{A/W}$  is measured for gold nanohole array device at  $1100\ \text{nm}$ . The ITO control device shows peak responsivity at  $\lambda = 980\ \text{nm}$  and a cutoff wavelength of  $\lambda = 1470\ \text{nm}$ . In contrast, the NP-PEPD has peak responsivity at  $\lambda = 1112\ \text{nm}$  with the same cutoff wavelength.

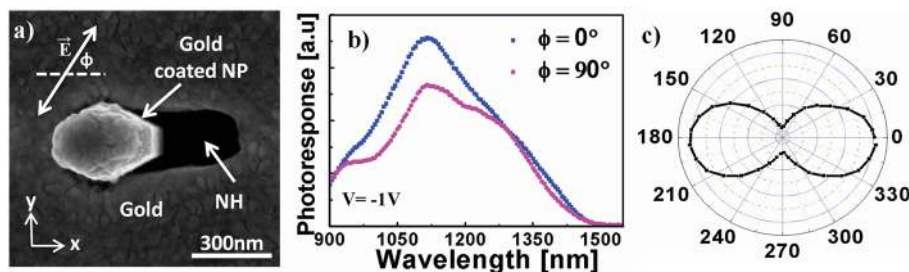


**Figure 3.** (a) High-resolution SEM of the NP in the nanohole (NH), and orientation of light polarization. (b) Photoresponse for  $x$ - and  $y$ -polarized light. (c) Polarization dependent photocurrent at 1100 nm showing  $\cos^2(\varphi)$  angular dependence.

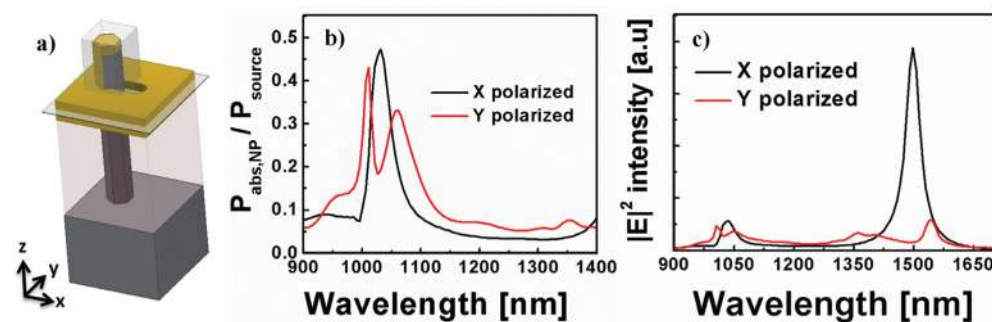


**Figure 4.** (a) Structure definition for 3D FDTD simulation. (b,c) FDTD simulation of the (b) power absorbed in the NP-PEPD for the  $x$ - and  $y$ -polarizations, and (c) electric field intensity.

The peak responsivity around  $\lambda = 1112$  nm is attributed to the resonant coupling of the  $SP_{(\pm 1, \pm 1)}$  modes into the NP. The lower responsivity of the NP-PEPD is attributed to the small spatial overlap between the NP-substrate depletion region and the e-field intensity “hot-spots” from the  $SP_{(\pm 1, \pm 1)}$  mode.

Effects of the asymmetric self-aligned nanohole are elucidated through polarization-specific spectral response of the NP-PEPD described in Figure 3a–c. As shown in Figure 3a, the polarization of light with respect to the long axis of the nanohole is considered  $x$ -polarized and the polarization orientation is delineated using angle  $\varphi$ . As shown in Figure 3b, the photoresponse of the NP-PEPD device when incident light is  $x$ -polarized light ( $\varphi = 0^\circ$ ) produces a higher photocurrent compared to the  $y$ -polarized light ( $\varphi = 90^\circ$ ) for much of the photoresponse spectrum, except at 1260 nm where the photocurrent for both polarizations is the same. It is interesting to note that the peak responsivity for both  $\varphi = 0^\circ$  and  $\varphi = 90^\circ$  occur at 1110 nm independent of polarization suggesting photoresponse enhancement due to  $SP_{(\pm 1, \pm 1)}$  mode. Figure 3(c) shows a polar plot of the photocurrent for incident wavelength at 1100 nm. The photocurrent is measured at the peak responsivity of  $\lambda = 1100$  nm from  $\varphi = 0$  through a full  $360^\circ$  revolution at  $10^\circ$  increments. The maximum photocurrent is measured for the  $x$ -polarization with a 25% drop in the photocurrent for  $y$ -polarized light. The photocurrent shows a  $\cos^2 \varphi$  dependence on the incident light polarization similar to the optical antenna behavior observed with gold nanorods.<sup>27</sup> In the case of the ITO control device, there is no dependence of the photoresponse on polarization [see Supporting Information]. This dipole-like dependence of the photocurrent is commonly attributed to the specific nature of the localized surface plasmon (LSP) that is excited in the gold nanohole.<sup>27–29</sup> However, the polarization dependence of the spectral response of the NP-PEPD

is the opposite expected of an elongated nanohole, where the maximum transmission occurs at  $\varphi = 90^\circ$  and the minimum at  $\varphi = 0^\circ$ .

To explain the experimental polarization dependence full wave finite difference time domain (FDTD) simulations are carried out on a 3D model of the NP-PEPD using the commercial software Lumerical. The incident plane wave is polarized in both the  $x$ - and  $y$ -polarizations over a wavelength range of 900–1600 nm. The 3D unit cell of the modeled structure is shown in Figure 4a. Periodic boundary conditions are implemented in the  $x$ - and  $y$ -boundaries with a pitch of  $1 \mu\text{m}$ . Perfectly matched layer (PML) boundary conditions are implemented in the  $z$ -directions.  $\text{In}_{0.4}\text{Ga}_{0.6}\text{As}$  optical parameters<sup>30</sup> are used to describe the NP, GaAs optical parameters<sup>31</sup> are used for the substrate. A fine mesh of  $1 \text{ nm} \times 1 \text{ nm} \times 2 \text{ nm}$  is used in the gold and the tip of the exposed nanopillar in contact with the gold.

The fractional power absorbed in the nanopillar is computed by numerically evaluating eq 2, where  $\varepsilon''(\omega)$  is the imaginary part of the dielectric constant of  $\text{In}_{0.4}\text{Ga}_{0.6}\text{As}$ , and  $|E(\omega, x, y, z)|^2$  is the electric field intensity. The integral is evaluated within the volume of the  $\text{In}_{0.4}\text{Ga}_{0.6}\text{As}$  nanopillar.

$$P_{\text{abs}}(\omega) = \iiint_{\text{NP2}} \frac{1}{2} \omega |E(\omega, x, y, z)|^2 \varepsilon''(\omega) dV \quad (2)$$

Figure 4b shows the spectra for the fractional power absorbed in the NP for the  $x$ - and  $y$ -polarizations respectively. For the  $x$ -polarization there is a peak at 1030 nm where 47% of the incident light is absorbed in the nanopillar, while for the  $y$ -polarization there are two peaks at 1010 and 1060 nm. The peaks at 1030 nm for the  $x$ -polarization and 1010 for the  $y$ -polarization are attributed to  $SP_{(\pm 1, \pm 1)}$  mode. These simulations shed light on the experimentally measured spectra in Figure 3b. The  $SP_{(\pm 1, \pm 1)}$

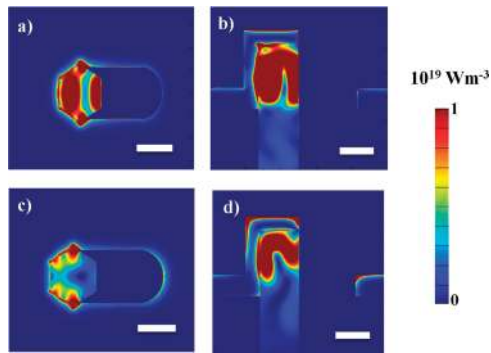


**Figure 5.** Spatial profile of the power absorbed in the structure for the  $x$ -polarization in the (a)  $x$ - $y$  plane and (b)  $x$ - $z$  plane. Spatial profile of the power absorbed in the structure for the  $y$ -polarization in the (c)  $x$ - $y$  plane and (d)  $x$ - $z$  plane. Scale bar is 200 nm.

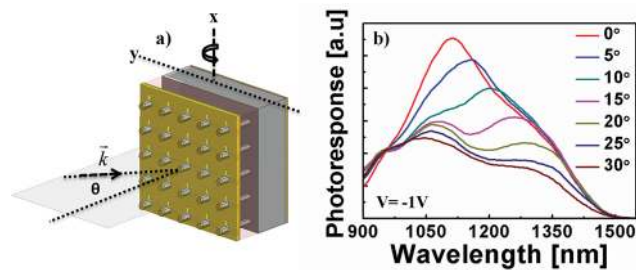


**Figure 6.** (a) Schematic of the sample orientation in the angle dependent photoresponse measurement. (b) Angular photoresponse of the gold nanohole array photodetector showing the shift and splitting of the  $SP_{1,1}$  resonance.

mode is excited in both the  $x$ - and  $y$ -polarizations, where it is stronger in the  $x$ - than the  $y$ -polarization.

Figure 4c shows the spectra for the electric field intensity integrated over the NP volume for the  $x$ - and  $y$ -polarizations respectively. Mirroring the calculated power absorption spectrum in Figure 4b, the  $SP_{(\pm 1, \pm 1)}$  are observed in the integrated electric field intensity for both the  $x$ - and  $y$ -polarizations. In addition, the  $x$ -polarization has an even stronger resonance at 1500 nm that is attributed to the  $SP_{(0, \pm 1)}$  resonance, which is largely absent for the  $y$ -polarization. However, this peak is not observed in the absorption spectra, as it lies at a longer wavelength than the cutoff of the InGaAs NPs at 1450 nm. The strong  $SP_{(0, \pm 1)}$  resonance is very encouraging for future NP-PEPD device demonstrations since greater optical coupling efficiency of the  $SP_{(0, \pm 1)}$  mode into the NP would result in a much higher responsivity.

Figure 5a–d shows the power absorption spatial profiles for the  $SP_{(\pm 1, \pm 1)}$  mode for the  $x$ - (at 1030 nm) and  $y$ - (at 1010 nm) polarizations. For the  $x$ -polarized illumination, the power absorption is tightly confined in the tip of the exposed nanopillar as shown in Figure 5a,b. Compared to the NP volume, there is relatively little absorption in the gold. For the  $y$ -polarization, the power absorption in the nanopillar is comparatively weaker, and more metal loss can be observed on the gold cap and nanohole edges. Hence, we expect that photogeneration within the semiconductor nanopillar at the  $SP_{(\pm 1, \pm 1)}$  mode will also be greater for the  $x$ -polarization compared to the  $y$ -polarization. These absorption profiles clearly explain why the experimentally measured polarization dependent spectral response does not follow

the transmission of an elongated nanohole. Because of the complex nanohole/NP geometry from the gold cap and non-conformally gold coated NP, light is focused into the nanopillar greater in the  $x$ -polarization.

Angular photoresponse characterization is used to confirm that the experimentally measured peak at 1110 nm is in fact the  $SP_{(\pm 1, \pm 1)}$  Bloch wave mode.<sup>32–34</sup> The in-plane momentum of the incident light varies as  $k_o \sin(\theta)$ , where  $\theta$  is the angle of incidence. As the in-plane momentum of the incident light is varied, the condition for momentum matching to SPP-BWs is changed. For a 2D plasmonic crystal with in-plane momentum in only the  $y$ -direction, the Bragg coupling condition is given by<sup>32</sup>

$$k_o \operatorname{Re} \left( \sqrt{\frac{\epsilon_m \epsilon_d}{\epsilon_m + \epsilon_d}} \right) = \left| \left( k_o \sin(\theta) \pm j \frac{2\pi}{P} \right) \hat{y} \pm i \frac{2\pi}{P} \hat{x} \right| \quad (3)$$

From eq 3, it can be seen that the  $SP_{(\pm 1, \pm 1)}$  degenerate modes will split into the  $SP_{(\pm 1, -1)}$  and  $SP_{(\pm 1, 1)}$  modes with increasing incident angle ( $\theta$ ). Qualitatively, as  $\theta$  is increased the  $SP_{(\pm 1, -1)}$  modes will red shift and the  $SP_{(\pm 1, 1)}$  modes will blue shift to satisfy momentum matching.

Figure 6a,b shows the schematic of the sample orientation for the angular photoresponse measurement and the angular photoresponse spectra. Light is polarized along the long axis of the nanohole ( $\phi = 0$ ). The NP-PEPD detector is placed on a 360° rotation mount with a minimum resolution of 2°, and rotated about the  $x$ -axis. At normal incidence ( $\theta = 0$ ) the  $SP_{(\pm 1, \pm 1)}$  modes are degenerate, which results in the peak at 1110 nm. As  $\theta$  is increased from 0–10°, the peak photoresponse at 1110 nm red shifts due to the  $SP_{(\pm 1, -1)}$  modes, and also broadens due to splitting of the  $SP_{(\pm 1, 1)}$  modes. At 15° it is clearly observed that the photoresponse spectrum has split into two peaks. These two clearly distinguishable peaks are due to the  $SP_{(\pm 1, 1)}$  modes at 1080 nm and  $SP_{(\pm 1, -1)}$  modes at 1270 nm. As the  $\theta$  is increased beyond 15°, the  $SP_{(\pm 1, 1)}$  modes blue shift further such that the peak responsivity is 1045 nm at  $\theta = 30^\circ$ . Angular photoresponse measurements thus confirm that the photoresponse peak at 1110 nm at normal incidence is due to the  $SP_{(\pm 1, \pm 1)}$  Bloch wave mode. FDTD simulations are also performed on the power absorbed in the nanopillar when the pitch of the square lattice is varied from 700–1200 nm. These simulations show that the absorption in the nanopillar follows the trend described by eq 1 for  $SP_{(\pm 1, -1)}$  mode supported by the gold/BCB interface (see Supporting Information).

These results strongly suggest a straightforward path for device improvement to improve the quantum efficiency and responsivity. First, the grating period can be reduced such that the  $SP_{(0, \pm 1)}$  resonance overlaps with the material absorption bandwidth. This will provide a much larger field enhancement within the nanopillar with increased photogeneration of carriers and better optical efficiency. Second, the nanopillar can be grown so that the photodetector junction has a stronger overlap with the field. In this initial demonstration, the p-n junction is located at the substrate/NP interface, far from the field enhancement. Instead, a core/shell p-n NP geometry, or Schottky junction can be used so that the photodetector junction extends the length of the NP and is strongly coupled to the plasmonic “hot-spot.” Third, this fabrication scheme is flexible, allowing variation of the NP-nanohole geometry by varying the angle of deposition, BCB thickness, and nanopillar height and diameter, in order to optimize the field enhancement and polarization sensitivity.

In summary, we have demonstrated a novel type of photo-detector based on surface plasmon field enhancements in NP arrays. In this initial proof-of-concept demonstration, we have shown that the responsivity spectrum can be engineered by using the metal nanohole array which acts as a 2D plasmonic crystal such that SPP-BWs couple light into the NP. The periodicity, metal nanohole shape, and metal dielectric function can be engineered to absorb light in different spectral ranges. FDTD modeling confirms the existence of electric field intensity hot spots in the nanopillar, and also provides a design scheme for higher responsivity photodetectors. NP-PEPDs can offer significant advantages over planar devices in terms of reduced leakage current and smaller capacitance due to their smaller footprint. NP-PEPDs have applications in plasmonically enhanced focal plane arrays and nanostructured photovoltaic devices.

## ■ ASSOCIATED CONTENT

**S Supporting Information.** Additional figures and information. This material is available free of charge via the Internet at <http://pubs.acs.org>.

## ■ AUTHOR INFORMATION

### Corresponding Author

\*E-mail: [pradeeps@ee.ucla.edu](mailto:pradeeps@ee.ucla.edu).

## ■ ACKNOWLEDGMENT

The authors gratefully acknowledge the financial support of this research by NSF (through ECCS-0824273, DMR-1007051, and DGE-0903720), AFOSR (FA9550-08-1-0198, FA9550-09-1-0270) and by DoD (through NSSEFF N00244-09-1-0091). The authors would also like to acknowledge the Integrated Systems Nanofabrication Cleanroom (ISNC) staff for assistance with wire bonding, and electron beam lithography via the Vistec EBPG 5000+ES.

## ■ REFERENCES

- (1) Kempa, T. J.; Tian, B.; Kim, D. R.; Hu, J.; Zheng, X.; Lieber, C. M. *Nano Lett.* **2008**, *8*, 3456–3460.
- (2) Lysov, A.; Vinaji, S.; Offer, M.; Gutsche, C.; Regolin, I.; Mertin, W.; Geller, M.; Prost, W.; Bacher, G.; Tegude, F.-J. *Nano Res.* **2011**.
- (3) Goto, H.; Nosaki, K.; Tomioka, K.; Hara, S.; Hiruma, K.; Motohisa, J.; Fukui, T. *Appl. Phys. Express* **2009**, *2* (2), 5004.
- (4) Colombo, C.; Hei, M.; Grätzel, M.; Morral, A. F. i. Gallium arsenide p-i-n radial structures for photovoltaic applications. *Appl. Phys. Lett.* **2009**, *94*, 173108.
- (5) Gunawan, O. G. O.; Wang, K.; Fallahzad, B.; Zhang, Y.; Tutuc, E.; Guha, S. *Prog. Photovoltaics* **2011**, *19*, 307–312.
- (6) Senanayake, P.; Lin, A.; Mariani, G.; Shapiro, J.; Tu, C.; Scofield, A. C.; Wong, P. S.; Liang, B. L.; Huffaker, D. L. *Appl. Phys. Lett.* **2010**, *97*, 3.
- (7) Soci, C.; Zhang, A.; Xiang, B.; Dayeh, S. A.; Aplin, D. P. R.; Park, J.; Bao, X. Y.; Lo, Y. H.; Wang, D. *Nano Lett.* **2007**, *7*, 1003–1009.
- (8) Vj, L.; Oh, J.; Nayak, A. P.; Katzenmeyer, A. M.; Gilchrist, K.; Grego, S.; Kobayashi, N. P.; Wang, S.; Talin, A. A.; Dhar, N. K.; Islam, M. M. *IEEE J. Sel. Top Quantum Electron.* **2011**, *17*, 1002–1032.
- (9) Gallo, E. M.; Chen, G.; Currie, M.; McGuckin, T.; Prete, P.; Lovergine, N.; Nabet, B.; Spanier, J. E. Picosecond response times in GaAs/AlGaAs core/shell nanowire-based photodetectors. *Appl. Phys. Lett.* **2011**, *98*, 241113.
- (10) Mariani, G.; Wong, P. S.; Katzenmeyer, A. M.; Leonard, F.; Shapiro, J.; Huffaker, D. L. *Nano Lett.* **2011**, *11*, 2490–2494.
- (11) Genet, C.; Ebbesen, T. W. *Nature* **2007**, *445*, 39–46.
- (12) Ebbesen, T. W.; Lezec, H. J.; Ghaemi, H. F.; Thio, T.; Wolff, P. A. *Nature* **1998**, *391*, 667–669.
- (13) Lee, S. C.; Krishna, S.; Brueck, S. R. J. *Opt. Express* **2009**, *17*, 23160–23168.
- (14) Ishi, T.; Fujikata, J.; Makita, K.; Baba, T.; Ohashi, K. *Jpn. J. Appl. Phys., Part 2* **2005**, *44*, L364–L366.
- (15) Shackelford, J. A. *Appl. Phys. Lett.* **2009**, *94*, 083501.
- (16) Tang, L.; Kocabas, S. E.; Latif, S.; Okyay, A. K.; Ly-Gagnon, D. S.; Saraswat, K. C.; Miller, D. A. B. *Nat. Photonics* **2008**, *2*, 226–229.
- (17) Tang, L.; Miller, D. A.; Okyay, A. K.; Matteo, J. A.; Yuen, Y.; Saraswat, K. C.; Hesselink, L. *Opt. Lett.* **2006**, *31*, 1519–1521.
- (18) Nakayama, K.; Tanabe, K.; Atwater, H. A. *Appl. Phys. Lett.* **2008**, *93*, 3.
- (19) Atwater, H. A.; Polman, A. *Nat. Mater.* **2010**, *9*, 205–213.
- (20) Munday, J. N.; Atwater, H. A. *Nano Letters* **2011**, *11*, 2195–2201.
- (21) Shapiro, J. N.; Lin, A.; Wong, P. S.; Scofield, A. C.; Tu, C.; Senanayake, P. N.; Mariani, G.; Liang, B. L.; Huffaker, D. L. *Appl. Phys. Lett.* **2010**, *97*, 243102–243102–3.
- (22) Chang, C.-Y.; Chang, H.-Y.; Chen, C.-Y.; Tsai, M.-W.; Chang, Y.-T.; Lee, S.-C.; Tang, S.-F. *Appl. Phys. Lett.* **2007**, *91*, 163107–3.
- (23) Chang, S.-H.; Gray, S.; Schatz, G. *Opt. Express* **2005**, *13*, 3150–3165.
- (24) Johnson, P. B.; Christy, R. W. *Phys. Rev. B* **1972**, *6*, 4370.
- (25) White, J. S.; Veronis, G.; Yu, Z.; Barnard, E. S.; Chandran, A.; Fan, S.; Brongersma, M. L. *Opt. Lett.* **2009**, *34*, 686–688.
- (26) Barnes, W. L.; Dereux, A.; Ebbesen, T. W. *Nature* **2003**, *424*, 824–830.
- (27) Knight, M. W.; Sobhani, H.; Nordlander, P.; Halas, N. J. *Science* **2011**, *332*, 702–704.
- (28) Koerkamp, K. J. K.; Enoch, S.; Segerink, F. B.; van Hulst, N. F.; Kuipers, L. *Phys. Rev. Lett.* **2004**, *92*, 4.
- (29) Degiron, A.; Ebbesen, T. W. *J. Opt. A: Pure Appl Opt.* **2005**, *7*, S90–S96.
- (30) Kim, T. J.; Ghong, T. H.; Kim, Y. D.; Kim, S. J.; Aspnes, D. E.; Mori, T.; Yao, T.; Koo, B. H. *Phys. Rev. B* **2003**, *68*, 10.
- (31) Adachi, S. *Properties of aluminium gallium arsenide* (INSPEC, 1993).
- (32) Gao, H.; Zhou, W.; Odom, T. W. *Adv. Funct. Mater.* **2010**, *20*, 529–539.
- (33) Williams, S.; Coe, J. *Plasmonics* **2006**, *1*, 87–93.
- (34) Chang, C.-C.; Sharma, Y. D.; Kim, Y.-S.; Bur, J. A.; Shenoi, R. V.; Krishna, S.; Huang, D.; Lin, S.-Y. *Nano Lett.* **2010**, *10*, 1704–1709.